

Supporting Information

Elucidation of the Intersystem Crossing Mechanism in a Helical BODIPY for Low-Dose Photodynamic Therapy

Zhijia Wang⁺, Ling Huang⁺, Yuxin Yan⁺, Ahmed M. El-Zohry, Antonio Toffoletti, Jianzhang Zhao, Antonio Barbon,* Bernhard Dick,* Omar F. Mohammed,* and Gang Han**

anie_202005269_sm_miscellaneous_information.pdf

Contents

1.0 Information for Triplet Photosensitizers.....	Page S2
2.0 Optical Spectra.....	Page S7
3.0 Intrinsic Triplet Lifetime.....	Page S8
4.0 Calculation of Triplet Quantum Yield.....	Page S10
5.0 TTA Upconversion Set-up and Quantum Yield.....	Page S12
6.0 Photodynamic Therapy.....	Page S15
7.0 Theroretical Computation and Coordinates of Optimized Geometries.....	Page S27
8.0 Time-resolved EPR spectroscopy of triplet states.....	Page S34
9.0 Synthesis and Molecular Structure Characterization Data.....	Page S38
10.0 References.....	Page S40

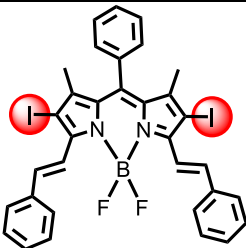
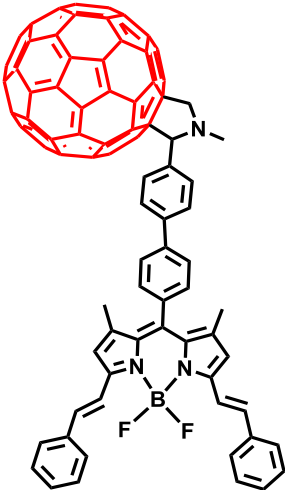
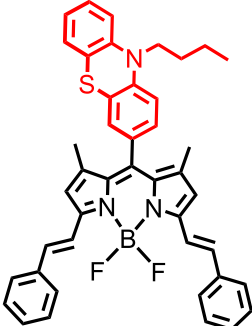
1.0 Information for Triplet Photosensitizers

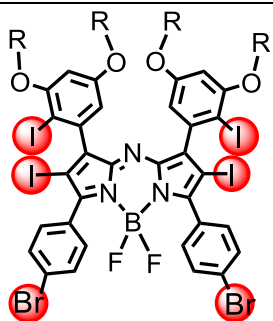
Table S1. Comparison of clinically approved PDT photosensitizers in oncology with **helical-BDP** in this paper.^[1]

	$\lambda_{\text{abs}}(\text{nm})^a$	$\varepsilon (\text{cm}^{-1}\text{M}^{-1})^b$	Drug dose ^c	Light dose ^d
Profimer sodium (Photofrin, HPD)	630	1170	1.5-2.5	50-500
ALA (precursor of PpIX)	635	<5000	30-60	-
Temoporfin (Foscan) (mTHPC)	652	30000	0.1	10
Talaporpin (NPe6)	664	40000	2.5	-
SnEt2 (Purlytin)	660		1.2	200
Lutetium Texaphyrin (Lu-tex)	732		0.6-7.2	150
Padoporfin (Tookad)	762	108600	2	23
Silicon phthalocyanine (Pc 4)	675		1	135
helical-BDP	630	176000	0.00025	6

^a Maximum absorption wavelength. ^b Molar extinction coefficient. ^c Drug dose, in mg/kg body weight. ^d Light dose, in J/cm².

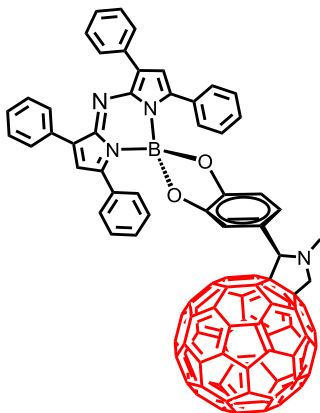
Table S2. Comparison of triplet lifetime of heavy atom (I, Br) and heavy atom-free long wavelength triplet photosensitizers.

Structure	Triplet lifetime	Reference
	$\tau_T = 1.7 \mu\text{s}$	<i>J. Mater. Chem. C</i> , 2014 , 2, 3900–3913
	$\tau_T = 72 \mu\text{s}$	<i>Org. Lett.</i> , 2012 , 14, 2594–2597
	$\tau_T = 391 \mu\text{s}$	<i>Chem. Commun.</i> , 2020 , 56, 1721–1724



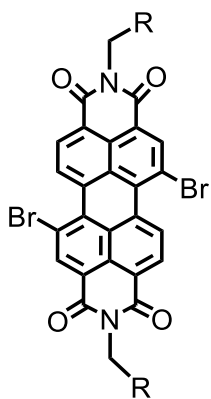
$\tau_T = 0.5 \mu\text{s}$

Chem.–Eur. J., **2012**, *18*, 12655–12662



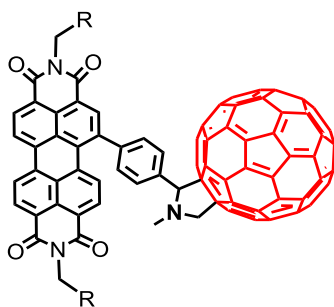
$\tau_T = 83 \mu\text{s}$

Chem. Commun., **2012**, *48*, 206–208



$\tau_T = 0.4 \mu\text{s}$

J. Phys. Chem. C, **2016**, *120*, 10162–10175



$\tau_T = 106 \mu\text{s}$

Chem. Commun., **2012**, *48*, 3751–3753

Table S3. Typical heavy atom-free triplet photosensitizers with different ISC mechanisms.

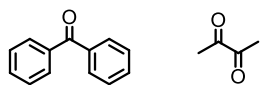
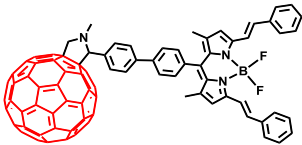
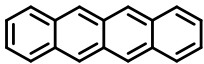
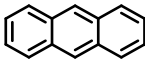
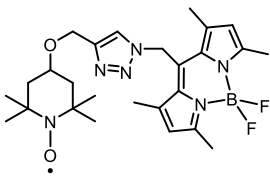
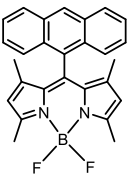
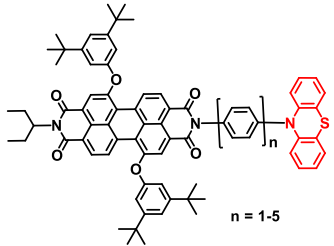
ISC mechanism	Exampler	Comments	Reference
$^1(n,\pi^*) \rightarrow ^3(\pi,\pi^*)$		Small molar extinction coefficient in visible light region	Principles of molecular photochemistry: an introduction, 2009
C₆₀ as spin converter		Molecular structure is complicated and with heavy molecular weight	<i>Org. Lett.</i> , 2012 , <i>14</i> , 2594–2597
Singlet fission		Low triplet energy level	<i>Chem. Rev.</i> , 2010 , <i>110</i> , 6891–6936
Energy matched S₁/T_n		Molecular structure Derivatization easily break energy matching	Principles of molecular photochemistry: an introduction, 2009
Radical enhanced ISC		The ISC efficiency and molecular structure relationship is unclear.	<i>J. Am. Chem. Soc.</i> , 2017 , <i>139</i> , 7831–7842
Spin-orbit charge transfer ISC		The ISC efficiency and molecular structure relationship is unclear.	<i>J. Am. Chem. Soc.</i> , 2017 , <i>139</i> , 6282–6285
Radical pair ISC		Molecular structure is complex, synthetic demanding	<i>J. Phys. Chem. B</i> , 2006 , <i>110</i> , 25163

Table S4. Comparison of **helical-BDP-NPs** and literature reported triplet photosensitizers for PDT augmented checkpoint blockade immunotherapy.

PSs	IC ₅₀ (μ M)	Drug dose ^a	Light dose ^b	Reference
helical-BDP	0.012	0.00025	6	This manuscript
Ce6	–	7.9 (<i>i.v.</i>)	30	<i>Biomaterials</i> , 2019 , 223, 119469
	–	5 (<i>i.v.</i>)	72	<i>ACS Nano</i> , 2019 , 13, 10242
	–	6 (<i>i.v.</i>)	18	<i>Adv. Funct. Mater.</i> , 2019 , 29, 1902440
Pheophorbide A	0.24	1.6 (<i>i.v.</i>)	65	<i>Biomaterials</i> , 2019 , 217, 119309
pyrolipid	0.42	6 (<i>i.v.</i>)	180	<i>J. Am. Chem. Soc.</i> , 2016 , 138, 16686
		1.4 (<i>i.v.</i>)	180	<i>Nat. Commun.</i> , 2016 , 7, 12499
IRDye 700	>>0.1	–	70	<i>Mol. Pharmaceutics</i> , 2019 , 16, 339
Porphyrin	~0.1	–	600	<i>Nanoscale</i> , 2018 , 10, 16738
5,10,15,20-tetra(p-benzoato)porphyrin	2.6	7.9 (<i>in situ</i>)	45	<i>J. Am. Chem. Soc.</i> , 2018 , 140, 5670

^a Drug dose, in mg/kg body weight. ^b Light dose, in J/cm²

2.0 Optical Spectra

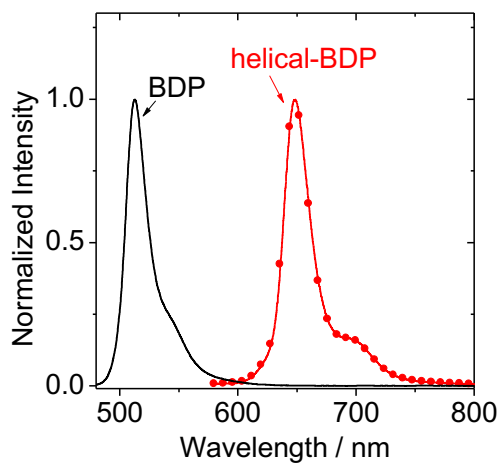


Figure S1. Normalized fluorescence emission spectra of **BDP** ($\lambda_{\text{ex}} = 470$ nm) and **helical-BDP** ($\lambda_{\text{ex}} = 570$ nm). $c = 1.0 \times 10^{-5}$ M in DCM, 20 °C.

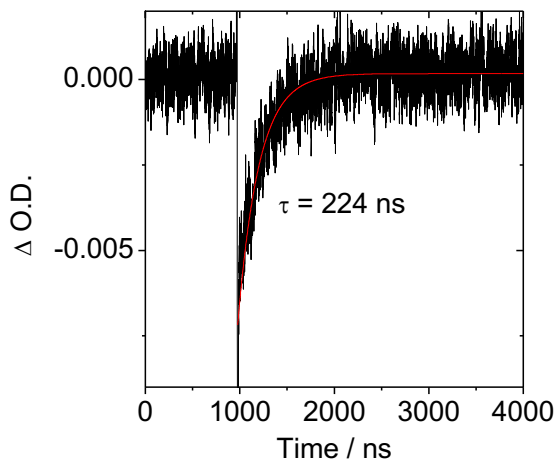


Figure S2. Decay trace of **helical-BDP** at 610 nm. $\lambda_{\text{ex}} = 628$ nm. $c = 3.1 \times 10^{-7}$ M in aerated DCM, recorded in the co-linear measurement mode of the LP980 ns-TA spectrometer. 20 °C.

3.0 Intrinsic Triplet Lifetime

When the intrinsic lifetime of the triplet states is long and the concentration of the triplet states is high, triplet-triplet annihilation is an additional contribution to the decay of the transient absorption.^[2] The corresponding differential equation for the triplet concentration^[3]

$$\frac{dc_T}{dt} = -k_1c_T - k_2c_T^2 \quad (\text{Eq. S1})$$

which has the solution as:

$$c_T(t) = \frac{c_0k_1}{\exp(k_1t) \cdot (c_0k_2 + k_1) - c_0k_2} \quad (\text{Eq. S2})$$

Where c_0 is the initial triplet concentration. This leads to the following expression for the transient absorption

$$A(t) = \frac{\frac{A_0\tau_2}{\tau_1}}{\exp\left(\frac{t}{\tau_1}\right) \cdot \left(1 + \frac{\tau_2}{\tau_1}\right) - 1} \quad (\text{Eq. S3})$$

Where A_0 is the initial transient absorption, $\tau_1 = 1/k_1$ is the intrinsic (unimolecular) lifetime of the triplet, and $\tau_2 = 1/c_0k_2$, which is the reciprocal of the initial concentration of triplets times the bimolecular rate constant of triplet triplet annihilation. We fitted the data sets (Figure S3a and S3b) of **helical-BDP** simultaneously by Eq. S3, with variation of all parameters (A_0 , τ_2), but with the intrinsic triplet lifetime (τ_1) constrained to the same value in all data sets.

The intrinsic triplet lifetime of **helical-BDP** is fitted to be 492 μs .

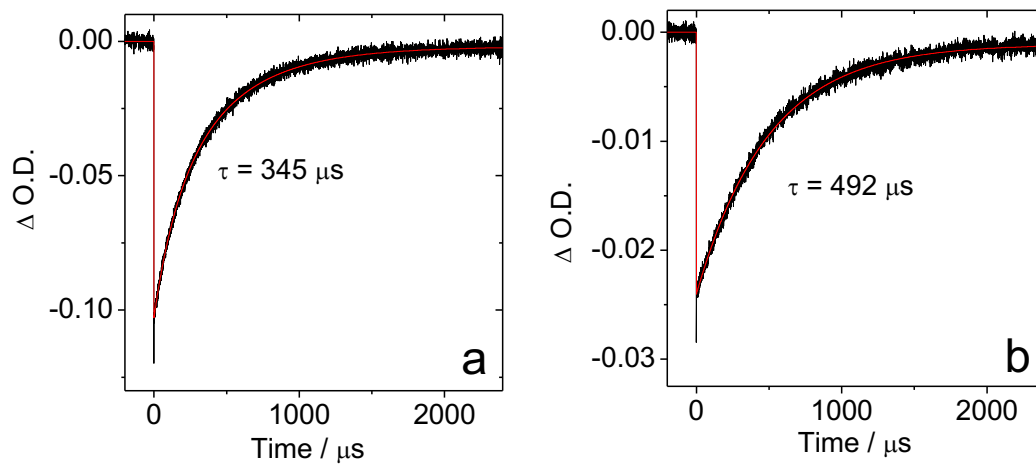


Figure S3. Triplet lifetimes of **helical-BDP** in deaerated toluene in different concentrations (a) $c = 1.3 \times 10^{-6}$ M (b) $c = 3.1 \times 10^{-7}$ M. The triplet lifetime values in each panel is fitted by LP900 software.

4.0 Calculation of Triplet Quantum Yield

The triplet quantum yield was determined by triplet-triplet energy transfer (TTET) method, using styryl-Bodipy as the triplet energy acceptor.^[4]

$$\Phi_{\text{T}}^{\text{sam}} = \Phi_{\text{T}}^{\text{ref}} \times \frac{\Delta A_{\text{sam}}}{\Delta A_{\text{ref}}} \times \frac{f_{\text{ref}}}{f_{\text{sam}}} \quad (\text{Eq. S4})$$

Where superscripts sam and ref designate sample and reference compound, respectively. Φ_{T} is the triplet quantum yield, ΔA is the transient absorption of the acceptor triplet formed by energy transfer from the donor, f is the triplet-triplet energy transfer efficiency.

Table S5. The value of the parameter.^a

	Δ O.D.	$k_{\text{obs}} / 10^6 \text{ s}^{-1}$	$k_0 / 10^6 \text{ s}^{-1}$	Φ_{T}
helical-BDP	0.0095	0.0685	0.0123	0.52 ^b
Methyl Blue	0.0093	0.1515	0.0217	0.50

^a The transient absorbance (Δ O.D.) of the styryl-BDP triplet, which was formed by energy transfer from **helical-BDP** or **Methyl Blue** triplet state, was monitored at 380 nm. k_{obs} is the pseudo-first-order rate constant for the growth of the styryl-BDP triplet, and k_0 is the rate constant for the decay of the donor triplets (in the absence of styryl-BDP) in solutions that contained **helical-BDP** or **Methyl Blue** at the same absorbance at the excitation wavelength. Φ_{T} stands for triplet quantum yield. ^b Calculated by Eq. S4. TTET efficiency is estimated to be

$$\frac{k_{\text{obs}}}{k_{\text{obs}} + k_0}$$

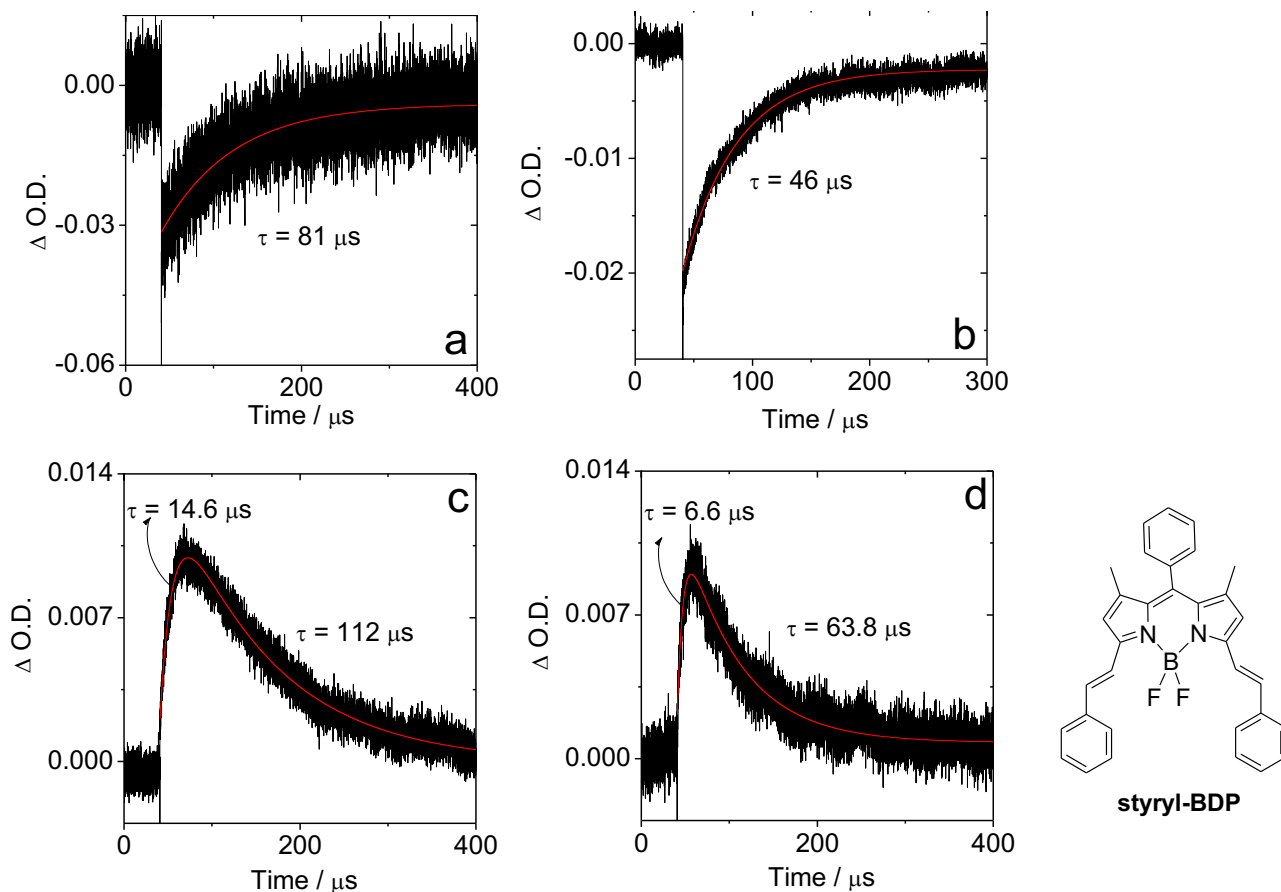


Figure S4. Nanosecond transient absorption spectra: (a) Decay trace of **helical-BDP** at 630 nm in DCM. (b) Decay trace of **Methyl Blue** at 600 nm in methanol. (c) Decay trace at 380 nm for **helical-BDP** mixed with styryl-BDP in DCM. (d) Decay trace at 380 nm for **Methyl Blue** mixed with styryl-BDP in methanol. The solutions in each figure show the same absorbance (0.35) at the excitation wavelength ($\lambda_{ex} = 601 \text{ nm}$), and the styryl-BDP is of the same quantity ($c = 1.0 \times 10^{-5} \text{ M}$). 20 °C.

5.0 TTA Upconversion Set-up and Quantum Yield

A continuous diode pumped solid-state laser (635 nm) was used as the excitation source for the upconversion. The laser spot was $1 \times 6 \text{ mm}^2$, and power of the laser beam was measured with VLP-2000 pyroelectric laser power meter. For the upconversion experiments, the mixed solution of the triplet photosensitizer and triplet acceptor was degassed with N_2 for at least 10 min, and gas flow was kept on during the measurement. The solution was excited with the laser, and the upconverted fluorescence was recorded with either a RF 5301PC spectrofluorometer or fiber spectrometer. In order to repress the laser scattering, a small black box was put behind the fluorescent cuvette to dump the laser. As there is strong inner filter effect due to the strong absorption of **helical-BDP**, a fiber was used to detect the strongest upconversion part in the edge (the set up is shown in Figure S5).

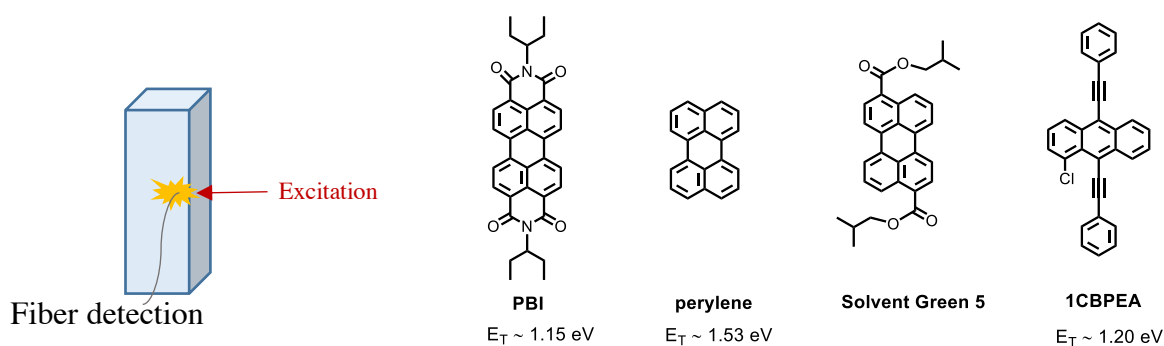


Figure S5. The set up for triplet-triplet annihilation (TTA) upconversion used in this study and the molecular structures of the acceptors.

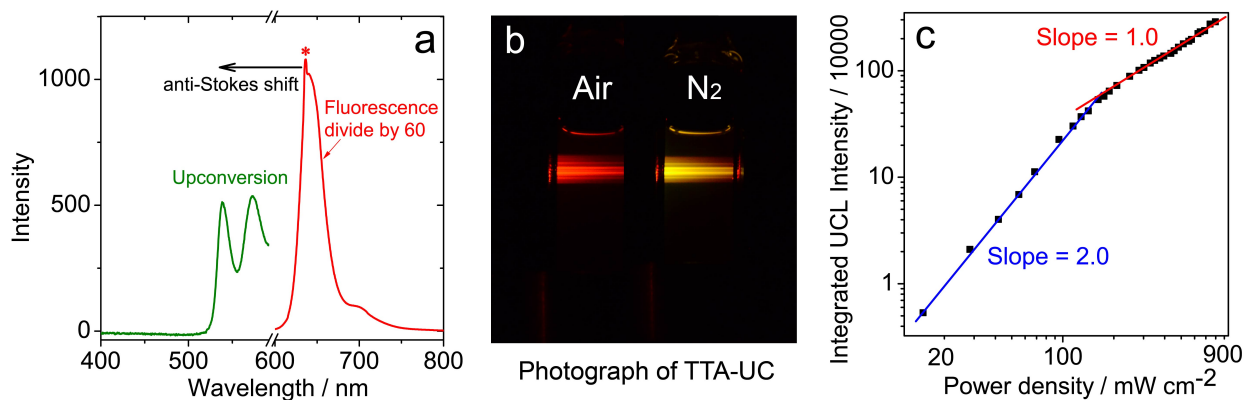


Figure S6. (a) Upconversion of **helical-BDP** and **PBI**. Excited with 635 nm cw-laser (250 mW/cm²). $c[\text{helical-BDP}] = 5.0 \times 10^{-6}$ M, $c[\text{PBI}] = 2.0 \times 10^{-4}$ M, in deaerated DCM. The fluorescence of **helical-BDP** was divided by 60, due to the much stronger fluorescence emission of **helical-BDP** ($\Phi_F = 21\%$). The spike marked with ‘*’ is due to the scatter of laser. (b) Photographs of the mixture of **helical-BDP** and **PBI** under air and N₂ atmosphere. A 490 – 600 nm bandpass filter was used before the camera. (c) Integrated upconversion intensity plotted as a function of incident power density. The transition threshold (I_{th}) between the quadratic and the linear ranges is determined to be 167 mW/cm².

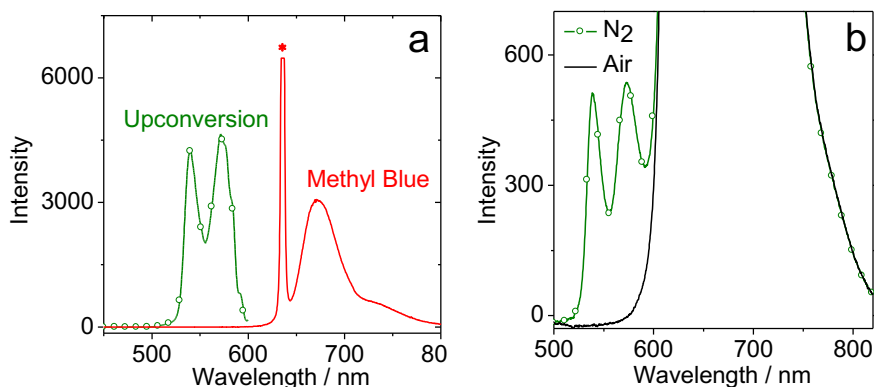


Figure S7. (a) Upconversion spectrum of **helical-BDP** with **PBI** (in deaerated DCM) and the emission of Methyl Blue (in MeOH) in same condition (Excited with 635 nm cw-laser (250 mW/cm²)). (b) Upconversion spectrum of **helical-BDP** with **PBI** in deaerated DCM, in air and in N₂. $c[\text{helical-BDP}] = 5.0 \times 10^{-6}$ M, $c[\text{PBI}] = 2.0 \times 10^{-4}$ M. The ‘*’ is due to the scatter of laser.

The triplet triplet annihilation upconversion quantum yield of the triplet photosensitizers were calculated according to literature method.^[5] The upconversion quantum yield (Φ_{UC}) was determined using the prompt fluorescence of **Methyl Blue** ($\Phi_F = 3\%$ in MeOH) as the standard.^[6] The upconversion quantum yield was calculated with following Eq. S5, where Φ_{UC} , A , I , and η represent the upconversion quantum yield, absorbance, integrated photoluminescence intensity, and refractive index of the solution. The subscripts sam and ref stand for sample and reference compound respectively. The equation is multiplied by a factor of 2 so as to set the maximum quantum yield to unity. The parameters for the upconversion quantum yield are shown in Table S6.

$$\Phi_{UC} = 2 \times \Phi_{ref} \times \frac{I_{sam}}{I_{ref}} \times \frac{1-10^{-A_{ref}}}{1-10^{-A_{sam}}} \times \left(\frac{n_{sam}}{n_{ref}}\right)^2 \quad (\text{Eq. S5})$$

Table S6. The value of the parameter.

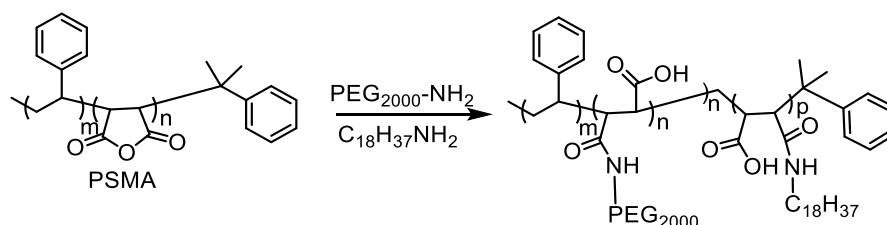
	A	I^a	Φ
Methyl Blue	0.037	1.69×10^6	$\Phi_F = 3\% ^b$
helical-BDP	0.708	1.90×10^6	$\Phi_{UC} = 0.8\% ^c$

^a Integrated photoluminescence intensity, calculated from Figure S7a; ^b Fluorescence quantum yield; ^c Upconversion quantum yield.

6.0 Photodynamic Therapy

Chemicals: Poly(styrene-co-maleic anhydride), cumene terminated Mn = 1900, PEG₂₀₀₀-NH₂ octadecylamine, tetrahydrofuran (THF), trimethylamine (TEA), *N,N*-dimethylformamide (DMF) were purchased from Sigma-Aldrich (St. Louis, MO, USA). Ultrapure water was prepared by using a Millipore Simplicity System (Millipore, Bedford, USA). All the above-mentioned chemicals were used as-received without further purification.

Scheme S1. The synthesis process of the polymer PSMA-PEG-OA.



An 50 mL dried round flask was charged with PSMA (160 mg), PEG₂₀₀₀-NH₂ (200 mg) and 30 mL dry THF. This flask was stirred under nitrogen and heated at 70 °C for 5 h. Then the octadecylamine (26 mg) was dissolved in dry THF (5mL), and slowly dropwise in 30 min. This reaction continues to stir for 5 hours at 70 °C. After the end of the reaction, use Hinsberg method to detect whether PEG₂₀₀₀-NH₂ and octadecylamine is over or not. When all the amines substrates were consumed, the reaction solution was transfer to a glass tube and store at 4 °C.

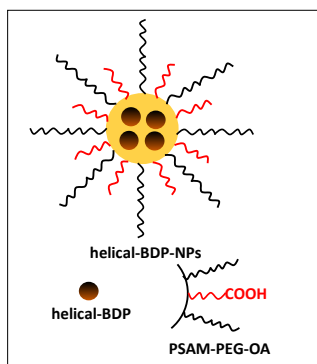


Figure S8. Illustration showing the structure of **helical-BDP-NPs**.

Synthesis of helical-BDP-NPs: 0.5 mg **helical-BDP**, and PSMA-PEG₂₀₀₀-OA (30 mg) were dissolved in 2 mL THF, and then 10 mL PBS buffer (pH = 7.24) were added. The mixture solution stirred in 40 °C for 2 h. The reaction mixture was cooled to room temperature and dialysis in DI water for 24 h. The **helical-BDP-NPs** were stored at 4 °C.

Loading percentage of helical-BDP in nanoparticles: After PSMA-PEG-OA encapsulated the **helical-BDP**, the **helical-BDP-NPs** was centrifuged (12000 × g), the precipitate was collected and then dissolved in DMF. The concentration was determined by UV-vis absorption spectra. The difference in absorption peak of **helical-BDP** before and after loading gives the mass of dye incorporated into the nanoparticles and can be calculated based on the standard curve created from the absorption spectra of standard **helical-BDP** solutions.

Entrapment efficiency (%) = weight of dye in nanoparticles/weight of dye fed initially × 100.

Characterization: UV-vis spectra were recorded on an Agilent Cary-5 spectrophotometer. Steady-state fluorescence spectra were measured on a HaiTech F-7000 fluorescence spectrometer (Xe lamp 500 W). The morphology of the **helical-BDP-NPs** nanoparticles was characterized by using a JEOL JEM-200CX transmission electron microscope (TEM) operated at 80 kV. The sample for TEM measurement was prepared by dropping the solution onto a carbon-coated copper grid, and 10 % sodium phosphotungstate aqueous solution negative staining the nanoparticles. The particle size of **helical-BDP-NPs** was measured by using dynamic light scattering (DLS) with a Zetasizer nano series analysis, the excitation wavelength is 532 nm.

Singlet oxygen generation under red LED irradiation: The singlet oxygen generation process was monitored by measurement the fluorescence of SOSG ($\lambda_{\text{ex}} = 450 \text{ nm}$). The mixture of **helical-BDP-NPs** (100 nM, 2mL PBS buffer) and SOSG (5 μM) was irradiated under 656 nm LED (5 mW/cm²). At the same time, the change of the fluorescence of SOSG is detected from 0 to 30 min.

Cell culture: Mice colon cancer (CT26 cell lines) and mice breast cancer cells (4T1 cell lines) were cultured in Dulbecco's modified Eagle's medium (DMEM) containing 10% fetal bovine

serum (FBS), 100 $\mu\text{g mL}^{-1}$ streptomycin, and 100 U mL^{-1} penicillin at 37 °C in a humidified incubator containing 5% CO_2 and 95% air. The medium was replenished every other day and the cells were subculture after reaching confluence.

Fluorescence imaging observed the cell uptake of helical-BDP-NPs: 100000 CT26 cells were planted to 35 mm confocal dish, and then incubated for other 12 hours. 100 nM **helical-BDP-NPs** was added into the 35 mm confocal dish. Then the intensity of intracellular fluorescence was measured at different time points (10, 30, 60, 90, 120, 180, 240 min) by laser scanning confocal microscope ($\lambda_{\text{ex}} = 630 \text{ nm}$). The fluorescence intensity in the cells was quantitatively analyzed (20 cells at each time point).

In vitro studies of helical-BDP-NPs mediated PDT in CT26 and 4T1 cell lines: The CT26 or 4T1 cells were planted in 96 well plate (1000 per well). After 24 hours, the **helical-BDP-NPs** (0, 6.25, 12.5, 25, 50, 100 nM) was added and continued to incubated 4 hours at 37 °C and 5% CO_2 . Then the cells were irradiated by using a red 656-nm LED for 60 min (5 min, 20 mW cm^{-2}). After irradiation the cells were again incubated for 24 h. Then, 20 μL of 5 mg mL^{-1} MTT solution in pH 7.4 PBS was added to each well. After 4 h incubation, the medium containing unreacted MTT was removed carefully, and 150 μL DMSO was added to each well to dissolve the produced blue formazan. After 30 minutes, the optical density (OD) at a wavelength of 595 nm was measured with a Bio-Rad microplate reader. The percentage of growth inhibition was calculated with Eq S6.

$$\text{Cell viability (\%)} = \text{OD value test} / \text{OD value control} \times 100 \% \quad (\text{Eq S6}).$$

SOSG monitor the production of singlet oxygen in cells under red light irradiation: 10^5 CT26 cells were planted to 35 mm confocal dish, and then incubated for other 12 hours. The mixture of **helical-BDP-NPs** (100 nM) and SOSG (5 μM) was added into the 35 mm confocal dish and incubated for 4 hours. After 5 min red LED irradiation (20 mW/cm^2 , 656 nm), the fluorescence of SOSG was measured in the cells by laser scanning confocal microscope ($\lambda_{\text{ex}} = 488 \text{ nm}$). The singlet oxygen quantum yield of **helical-BDP-NPs** in PBS buffer was determined with **Methyl Blue** ($\Phi_{\Delta} = 60\%$ in water) as the standard.

Propidium Iodide (PI) and Calcein A.M. staining the dead and living cells: The CT26 cells (1×10^5) per well were seeded on a confocal dish (35 mm) and incubated in complete medium for 12 h at 37 °C. The medium was then replaced with fresh culture medium containing **helical-BDP-NPs** (100 nM), to incubate for 4 hours at 37 °C. The cells were irradiated with red 656 nm LED for 5 min (20 mW cm^{-2}). After irradiation the cells were again incubated for 24 h. Afterward, the cells were stained with PI and calcein A.M. according to the manufacturer's instruction. After 20 min, the solution was removed and PBS was used to wash cells at least three times. The dead cells were visualized with a laser scanning confocal microscope (40 × oil objective), excitation wavelength was 549 nm, emission detection wavelength region was 580–620 nm. The living cells were also observed; the excitation wavelength was 488 nm, the emission was 500–550 nm.

Flow cytometry test the immune cells: The respective animal protocol has been approved by University of Massachusetts-Medical School. The spleen and tumor (right and left side) were isolated from the mice after different treatments. The tumor tissue was divided into small pieces, treated with 1 mg ml^{-1} collagenase I (Gibco) for 1 h at 37 °C and ground using the rubber end of a syringe (BD, 10 mL syringe). Cells were filtered through nylon mesh filters (Corning, cell strainer, 70 μm nylon). The single cells were collected by centrifugation ($800 \times g$, 5 min), the blood cells in the tumor tissue was eliminated by cold NH_4Cl lysis. The single suspensions tumor cells were washed by cold PBS containing 2 % FBS. In order to single suspensions immune cells from spleen, we grinded the spleen and cells were filtered by nylon mesh filters. The blood cells were lysis by twice NH_4Cl solution, and then washed with cold PBS containing 2% FBS. The tumor cells and immune cells from spleen were stained with fluorescence-labeled antibodies PerCP-Cy[™]5.5 Hamster Anti-Mouse TCR β chain (BD bioscience, clone H57-597, catalog No.560657), PerCP-Cy[™]5.5 Rat Anti-Mouse CD3 Molecular Complex Clone (BD bioscience, catalog No.560527), Pacific Blue[™] Rat Anti-Mouse CD45R (clone RA3-6B2, BD bioscience, catalog No. 558108), PE-Cy[™]7 Rat Anti-Mouse CD4 (Clone GK1.5, BD bioscience, catalog No.563933), PE Rat Anti-Mouse CD8a (Clone 53-6.7, BD bioscience, catalog No. 553032), APC Mouse Anti-Mouse NK-1.1 (Clone PK136, BD biosciences, catalog No.561117), FITC Rat Anti-Mouse CD44 (Clone IM7, BD biosciences, catalog No. 561859) , APC-Cy[™]7 Rat Anti-Mouse CD62L (Clone MEL-14, BD

biosciences, catalog No.560514) following the manufacturer's instructions. All antibodies were diluted 200 times. The stained cells were measured on a CytoFLEX flow cytometer (Beckman) and analyzed by FlowJo software (version 10.0.7, TreeStar).

Statistical analyses: The results are showed as the mean \pm standard error of the mean (s.e.m.), Moreover, Student's t-test was used for two-group comparisons. The Origin 9.0 was used to all statistical analyses. The threshold for statistical significance was *** $p < 0.001$, ** $p < 0.01$, or * $p < 0.05$.

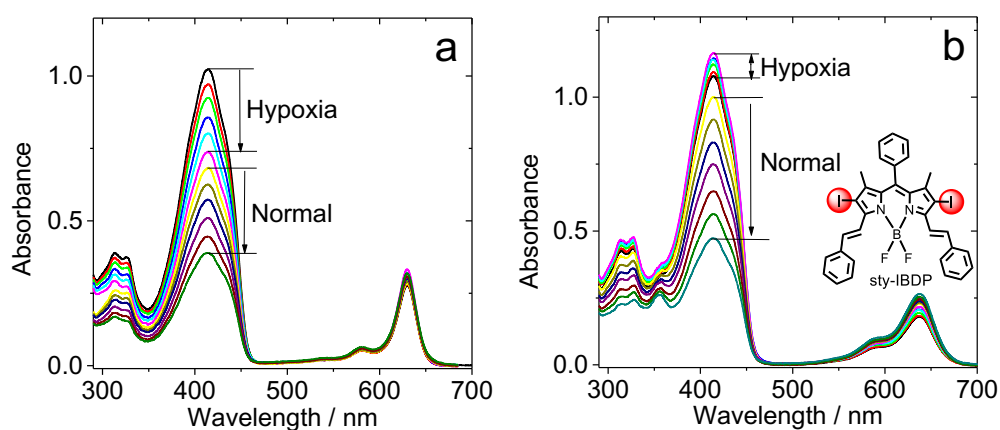


Figure S9. UV-Vis absorption changes for the 1,3-diphenylisobenzofuran (DPBF, ¹O₂ scavenger) with (a) **helical-BDP** ($\tau_T = 492 \mu\text{s}$) (b) **sty-IBDP** ($\tau_T = 1.7 \mu\text{s}$) as triplet photosensitizers in hypoxia atmosphere (0.2% O₂) and normal atmosphere (in air, 21% O₂) in DCM. The time interval of each spectrum is 30 s (irradiation time), except for the hypoxia region in (b) where the time interval is 60 s. The increase of the absorption in the 600–700 nm range is due to the evaporation of DCM. Note that for the determination of Φ_Δ , the same amount of DPBF was used for hypoxia atmosphere and normal atmosphere.

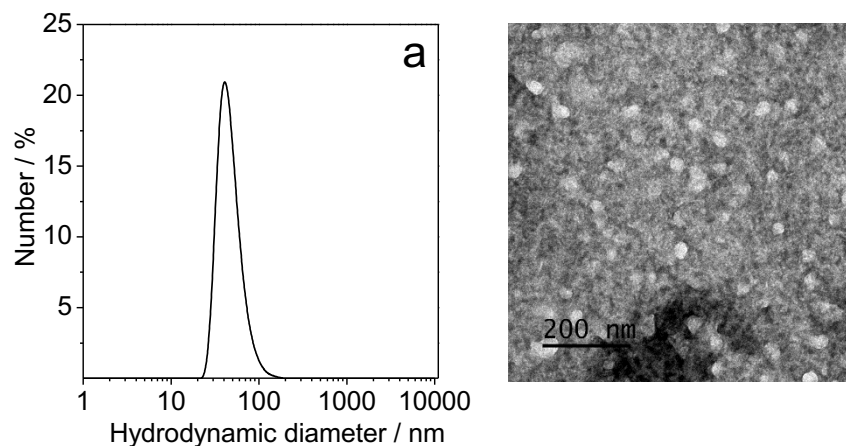


Figure S10. (a) The hydrodynamic diameter of **helical-BDP-NPs** in PBS via dynamic light scattering (DLS). (b) TEM image of **helical-BDP-NPs** stained by (10%) sodium phosphotungstate, scale bar represents 200 nm.

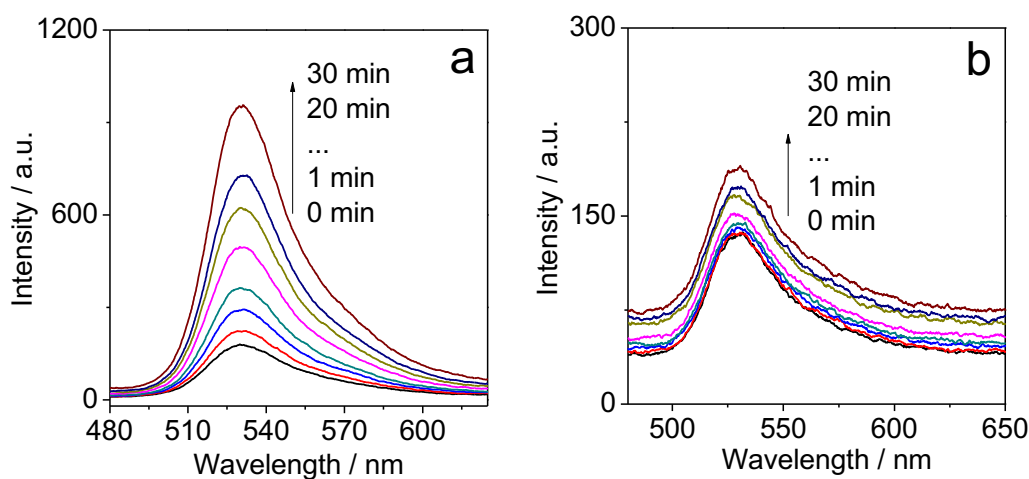


Figure S11. SOSG monitor $^1\text{O}_2$ generation for **helical-BDP-NPs** in PBS buffer. (a) **helical-BDP-NPs** ($c = 100 \text{ nM}$) and SOSG ($c = 5 \text{ }\mu\text{M}$); (b) only SOSG ($c = 5 \text{ }\mu\text{M}$). Irradiation condition: 656 nm LED, $5 \text{ mW}/\text{cm}^2$.

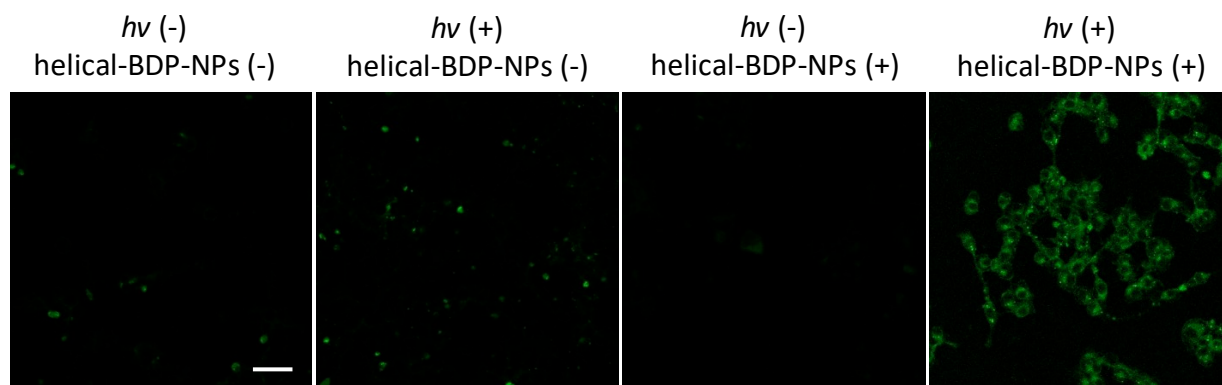


Figure S12. SOSG monitor singlet oxygen generation intracellular CT26 in different conditions. 656 nm LED irradiation, light dose: 6 J/cm². Scale bar is 50 μ m.

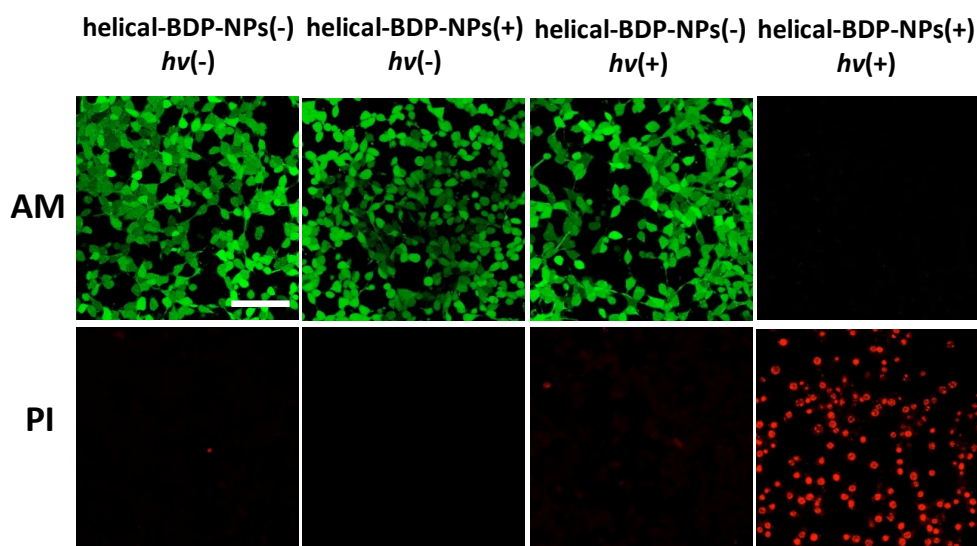


Figure S13. Calcein AM/propidium iodide (PI) staining cells to differentiate living or dead cells under different conditions. Capture wavelength of the fluorescence of PI (580 – 630 nm), $\lambda_{\text{ex}} = 561$ nm; capture wavelength of the fluorescence of AM (480 – 520 nm), $\lambda_{\text{ex}} = 476$ nm. $c[\text{helical-BDP-NPs}] = 100$ nM. Irradiation by 656 nm LED, light dose: 6 J/cm², 20 $^{\circ}$ C. The scale bar represents 100 μ m.

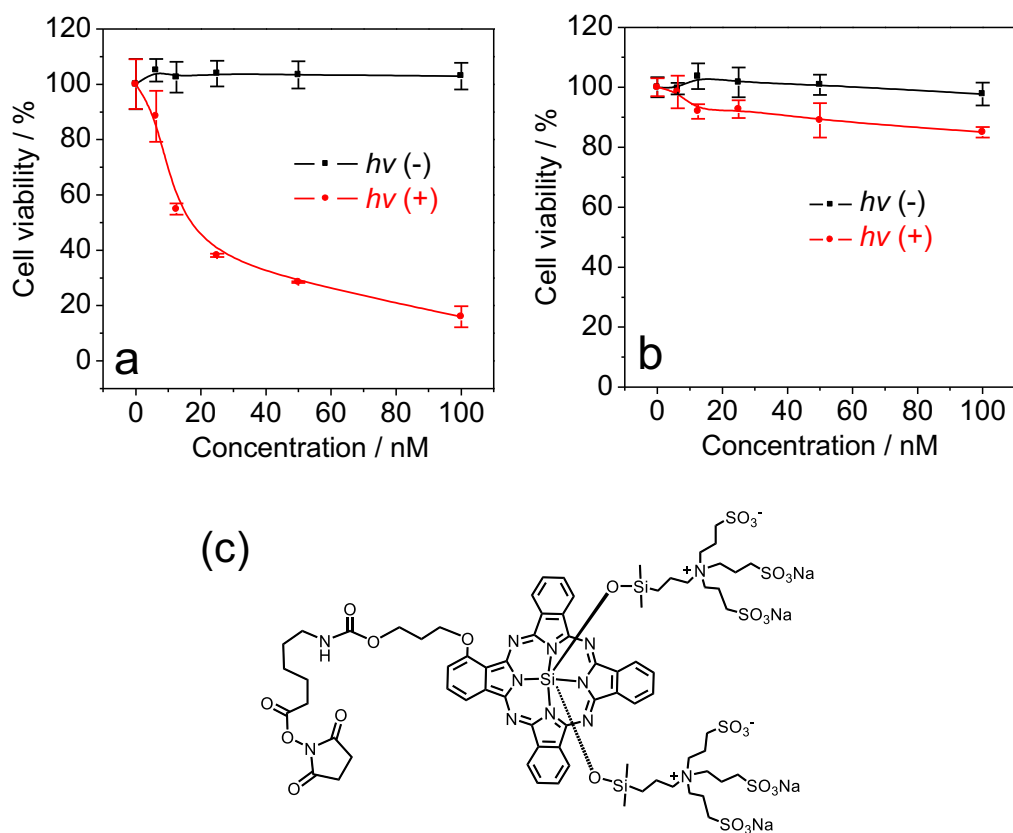


Figure S14. Comparison of cell viability of 4T1 cells pre-treated with increasing doses of (a) **helical-BDP-NPs** and (b) **IRDye 700DX** with and without light irradiation. (c) Molecular structure of **IRDye 700DX**. Irradiation condition: 656 nm for **helical-BDP-NPs** and 710 nm for **IRDye 700DX**, light dose: 6 J/cm². 20 °C.

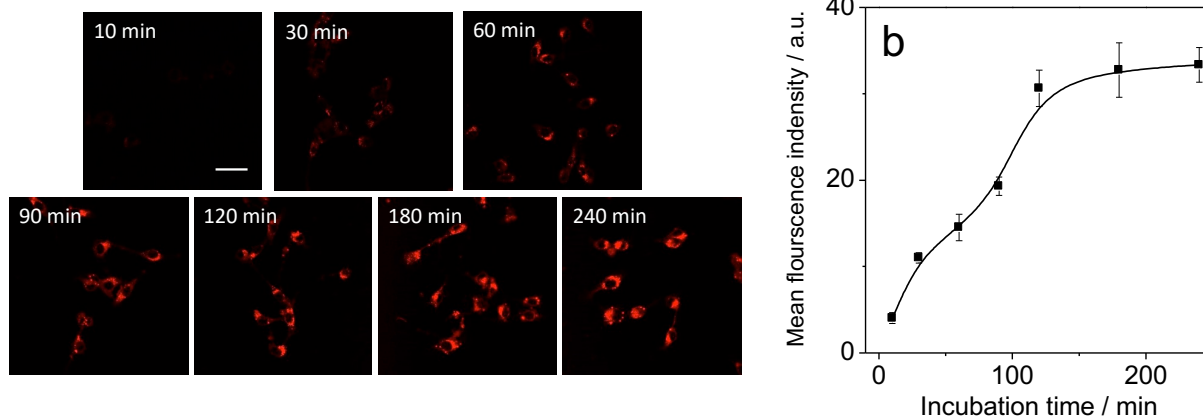


Figure S15. (a) Cell uptake of **helical-BDP-NPs** process by confocal microscopy observed for 240 min. $\lambda_{\text{ex}} = 561 \text{ nm}$, scale bar: $40 \mu\text{m}$. (b) Quantitative analysis of the fluorescence intensity of intracellular **helical-BDP**, $n = 10 \sim 15$ cells.

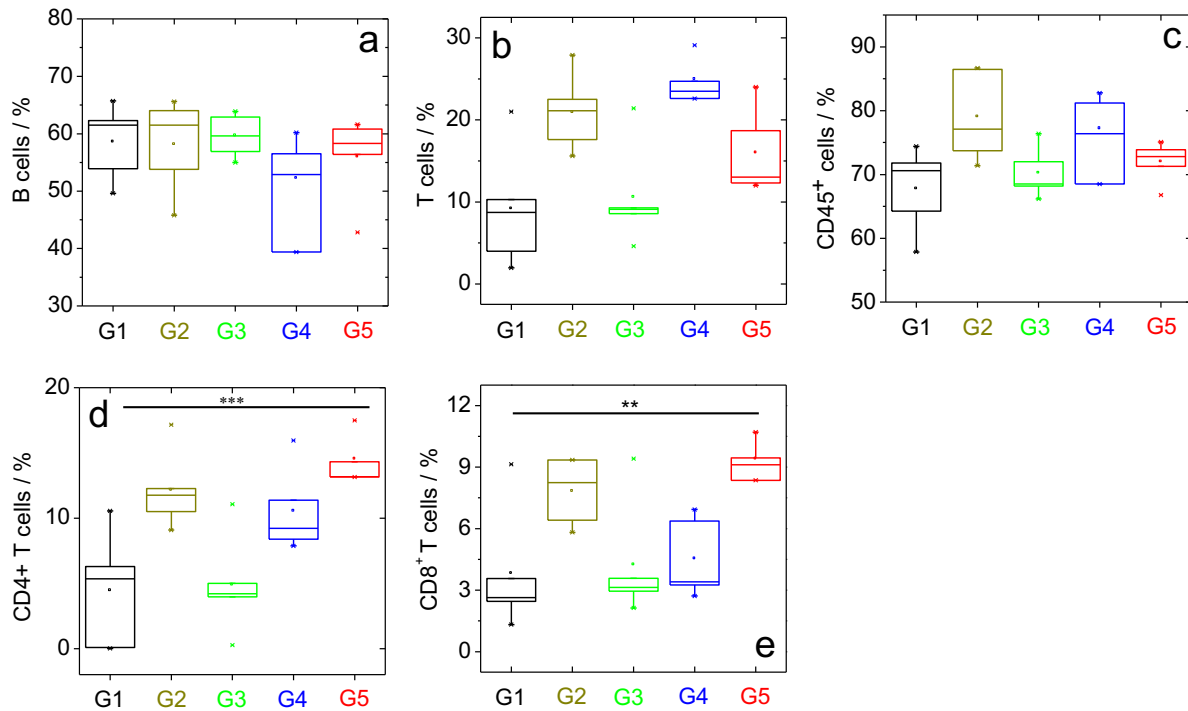


Figure S16. Analysis the immunity cells of spleen. (a) the percentage of B cells; (b) the percentage of T cells; (c) the percentage of CD45⁺ cells; (d) CD4⁺ T cells (e) CD8⁺ T cells in the spleen; Data are expressed as means \pm s.d. (n = 5). *P < 0.05, **P < 0.01, and ***P < 0.001.

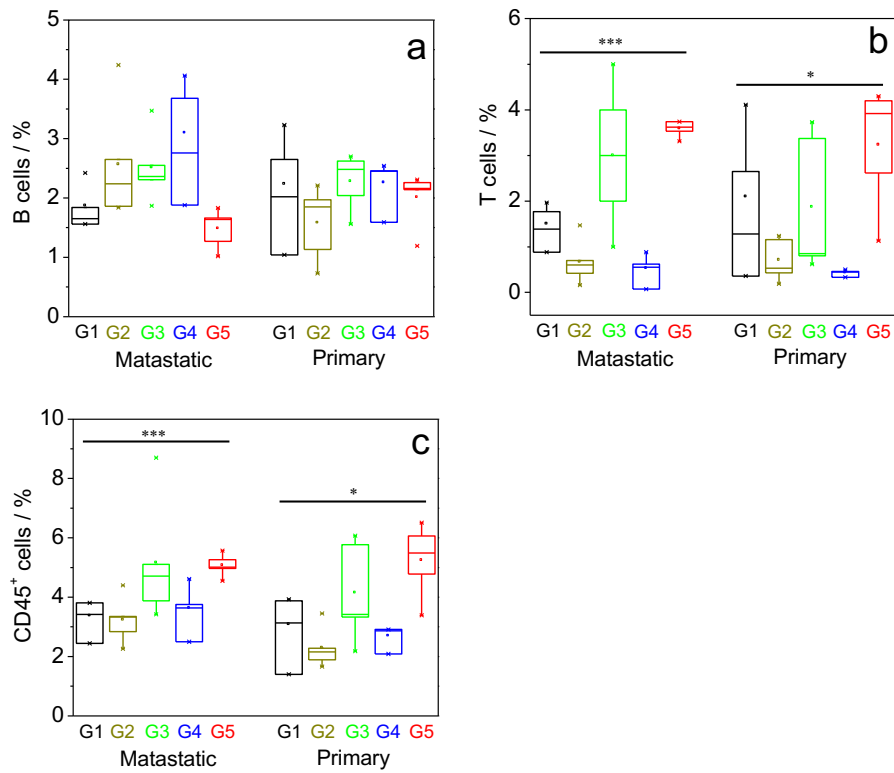


Figure S17. Analysis the immunity cells of metastatic tumor and primary tumor. The percentage of (a) B cells, (b) T cells and (c) CD45⁺ cells. Data are expressed as means \pm s.d. (n = 5). *P < 0.05, **P < 0.01, and ***P < 0.001.

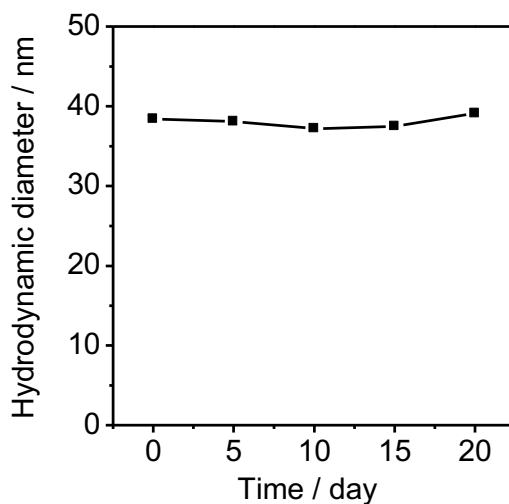


Figure S18. Hydrodynamic diameter of helical-BDP-NPs in PBS buffer for 20 days.

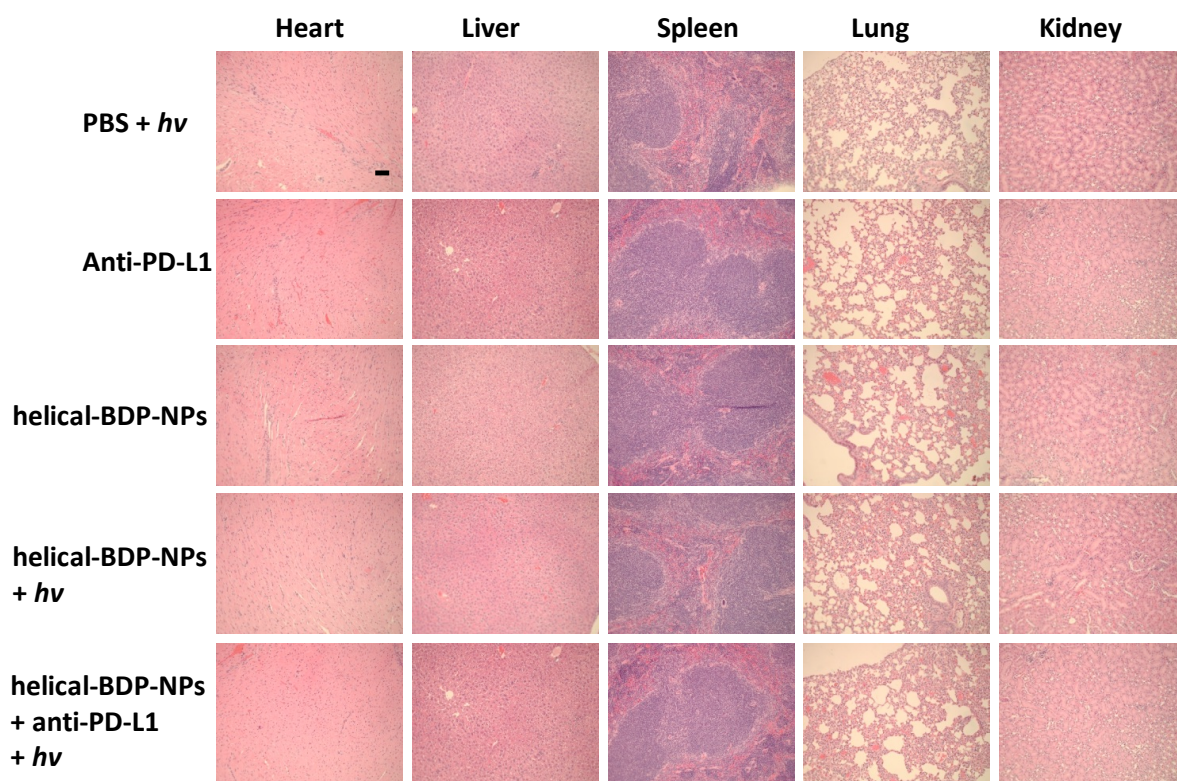


Figure S19. H&E stained images of tissue sections from different organs of mice. Scale bars: 100 μm .

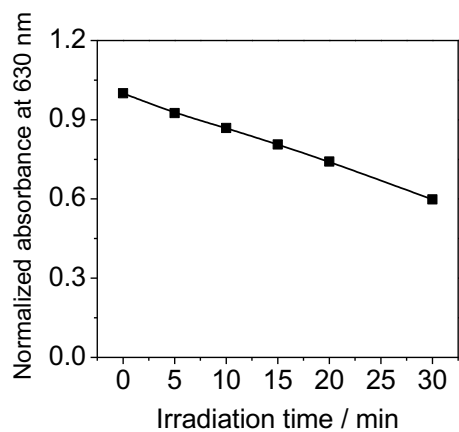


Figure S20. Photostability of **helical-BDP-NPs** in PBS buffer. Power intensity: 20 mW/cm^2 , 656 nm.

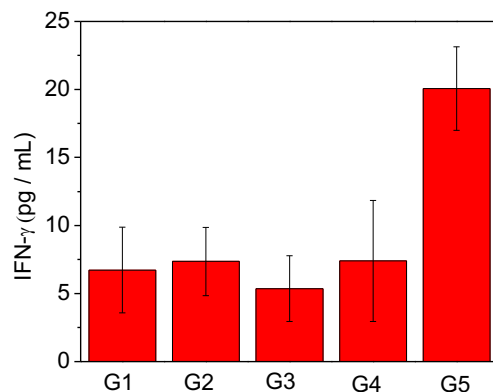


Figure S21. The concentration of IFN- γ in the in-mouse serum under different conditions. G1 ($h\nu$), G2 (anti-PD-L1), G3 (**helical-BDP-NPs** only), G4 (**helical-BDP-NPs** + $h\nu$), G5 (**helical-BDP-NPs** + $h\nu$ + anti-PD-L1).

7.0 Theroretical Computation and Coordinates of Optimized Geometries

Quantum Chemical Computations. All geometries were optimized with RHF wavefunctions and cc-pVDZ basis. The RHF molecular orbitals were subsequently used as the basis for a CAS-CI calculation that yields wavefunctions and energies for the excited states. The SOC matrix elements were calculated from these wavefunctions with the one-electron Breit-Pauli operator. All calculations were performed with the Firefly QC package,^[7] which is partially based on the GAMESS (US)^[8] source code. Vertical excitation energies and SOC couplings were calculated with a CI-calculation, using CAS (8,8) for **BDP** and CAS (12,12) for **helical-BDP**. Spin density distribution was obtained using the optimized triplet state geometry, calculated by DFT//B3LYP/6-31G(d).

Symmetry selection rules for spin-orbit coupling

The probability of a transition from a singlet state $|S\rangle$ to a triplet state $|T\rangle$ is proportional to the square of the spin-orbit coupling (SOC) matrix element:

$$\langle Sm_S | H^{SO} | Tm_T \rangle \quad (\text{Eq S7}).$$

In this expression, H^{SO} is the spin orbit coupling operator. It has dimension of energy, and involves both spatial and spin coordinates. It is invariant against all symmetry operations of the molecule, i.e. it belongs to the totally symmetric representation Γ_0 . The symbols S and T represent the spatial wavefunction of the singlet and triplet state, respectively. Their behavior with respect to symmetry operations are given by the symmetry representations Γ_S and Γ_T . When both states belong to the same symmetry representation, the product of the two spatial wavefunctions is totally symmetric. This is in particular the case when both states originate from the same orbital excitation (e.g. HOMO \rightarrow LUMO.)

Since the SOC matrix element is an integral over spatial and spin coordinates, the spin-function of the two states must be included. In the formula these are represented by the magnetic spin quantum number m . Whereas the only possible value for the singlet state is $m_S = 0$, the triplet has three spin functions characterized by $m_T = -1, 0, 1$. When zero-field splitting is accounted for, the eigenstates are usually labeled by $m_T = x, y, z$. (I.e., we must actually calculate three SOC matrix elements).

As a general rule, an integral like the SOC matrix element vanishes unless the function over which the integral is formed transforms like the totally symmetric representation. I.e., if the function is antisymmetric with respect to any one symmetry operation, the integral yields zero. The function in the integral is the product of the spatial wavefunctions, the spin wavefunctions, and the spin-orbit operator. This product transforms like the product of the corresponding representations:

$$\Gamma_{SOC} = \Gamma_S \times \Gamma_{m_S} \times \Gamma_{SO} \times \Gamma_T \times \Gamma_{m_T} = \Gamma_0 \quad (\text{Eq S8}).$$

This can be evaluated if the symmetry properties of the spin functions in the particular molecular point group are known. The spin function of a singlet state is totally symmetric,

and the three spin functions of the triplet state transform like the rotation operators around the x-, y-, and z-axis.

$$\Gamma_{m_S} = \Gamma_0 \quad (\text{Eq S9})$$

$$\Gamma_{m_T} = \{ \Gamma_{R_x}; \Gamma_{R_y}; \Gamma_{R_z} \} = \Gamma_{\mathbf{R}} \quad (\text{Eq S10})$$

In the particular case that the spatial wavefunctions of singlet and triplet state belong to the same symmetry representation, Eq. S8 simplifies to

$$\Gamma_{SOC} = \Gamma_{m_T} = \Gamma_0 = \Gamma_{\mathbf{R}} \quad (\text{Eq S11})$$

This means: Only those spin-substates of the triplet that transform like one of the three rotations can couple to the singlet state.

In the point group C_2 , only the rotation around the two-fold molecular axis is totally symmetric. Hence only the SOC matrix element for the spin-substate transforming like this axis is non-zero. I.e., if the two-fold axis is the z-axis, only T_z can couple. In the point group C_s , only the rotation around the axis perpendicular to the mirror plane is totally symmetric. If this is the z-axis, only T_z can couple. In the point groups C_{2v} and C_{2h} , none of the rotations are totally symmetric. Hence SOC between singlet and triplet is forbidden.

Table S7. Absolute energies (in Hartree units), energy differences (in units of cm^{-1}), and excitation wavelengths (in nm) from CAS-CI calculations at the RHF-optimized ground state structures. Note that CAS-CI calculations on this level of approximation strongly overestimate all excitation energies.

Sym.	helical-BDP			BDP
	C_{2v}	C_2	C_S	C_{2v}
RHF	-1595.837827	-1595.844817	-1595.844444	-1063.288782
CI-S ₀	-1595.875701	-1595.882245	-1595.882881	-1063.313277
CI-S ₁	-1595.748573	-1595.755533	-1595.755529	-1063.156152
CI-T ₁	-1595.800700	-1595.805896	-1595.805999	-1063.227993
CI-T ₂	-1595.743068	-1595.750242	-1595.750881	-1063.153169
CI-T ₃	-1595.736298	-1595.743101	-1595.743307	-1063.147340
S ₁ -S ₀ cm^{-1}	27901.4	27810.2	27950.5	34484.9
T ₁ -S ₀ cm^{-1}	16460.8	16756.8	16873.7	18717.8
S ₁ -S ₀ nm	358.4	359.6	357.8	290.0
T ₁ -S ₀ nm	607.5	596.8	592.6	534.3
S ₁ -T ₁ cm^{-1}	11440.6	11053.4	11076.9	15767.1
S ₁ -T ₂ cm^{-1}	-1208.2	-1161.3	-1020.1	-654.7
S ₁ -T ₃ cm^{-1}	-2694.0	-2728.4	-2682.5	-1934.1

helical-BDP

Symmetry: C₂

C	-1.216363051600	0.122150338800	0.497669401600
C	1.216363051600	-0.122150338800	0.497669401600
N	-1.230240355700	0.050663698900	-0.889189101600
N	1.230240355700	-0.050663698900	-0.889189101600
B	0.000000000000	0.000000000000	-1.819507793200
C	0.000000000000	0.000000000000	1.191541430700
C	-2.557155107600	0.286330754300	0.950822378100
C	2.557155107600	-0.286330754300	0.950822378100
C	-3.364821944800	0.251814319200	-0.194265689500
C	3.364821944800	-0.251814319200	-0.194265689500
F	-0.046531484800	-1.130151893000	-2.628679358900
F	0.046531484800	1.130151893000	-2.628679358900
C	-2.489031465600	0.127644043200	-1.297908172600
C	2.489031465600	-0.127644043200	-1.297908172600
C	-4.802103309900	0.326135844100	-0.426790198300
C	4.802103309900	-0.326135844100	-0.426790198300
C	-5.235578680200	0.330094046700	-1.770741390500
C	5.235578680200	-0.330094046700	-1.770741390500
C	-4.276976980900	0.231827090200	-2.854936874500
C	4.276976980900	-0.231827090200	-2.854936874500
C	-2.953368549400	0.120388571000	-2.653267387100
C	2.953368549400	-0.120388571000	-2.653267387100
C	-6.606987619800	0.405646826700	-2.063466808900
C	6.606987619800	-0.405646826700	-2.063466808900
C	-7.546105337200	0.463360751100	-1.062412927300
C	7.546105337200	-0.463360751100	-1.062412927300
C	-7.123802747500	0.434033480000	0.269442622700
C	7.123802747500	-0.434033480000	0.269442622700
C	-5.784460774000	0.363284474400	0.580327268900
C	5.784460774000	-0.363284474400	0.580327268900
C	0.000000000000	0.000000000000	2.686851330400
C	-3.060462842400	0.533428626900	2.345708177300
C	3.060462842400	-0.533428626900	2.345708177300
C	-0.372490031800	-1.143204781400	3.385712415400
C	0.372490031800	1.143204781400	3.385712415400
C	-0.365672465600	-1.144300842500	4.773264608500
C	0.365672465600	1.144300842500	4.773264608500
C	0.000000000000	0.000000000000	5.469584347500
H	-4.664859765000	0.238137776300	-3.865172654900
H	4.664859765000	-0.238137776300	-3.865172654900
H	-2.251331237600	0.033524996300	-3.466049967600
H	2.251331237600	-0.033524996300	-3.466049967600

H	-6.919199520800	0.412659050400	-3.099757464400
H	6.919199520800	-0.412659050400	-3.099757464400
H	-8.599257884300	0.520340160800	-1.301270717100
H	8.599257884300	-0.520340160800	-1.301270717100
H	-2.277484814700	0.829423463000	3.029279871400
H	2.277484814700	-0.829423463000	3.029279871400
H	-3.797581893100	1.334850146800	2.322438121400
H	3.797581893100	-1.334850146800	2.322438121400
H	-3.544887329300	-0.356802645000	2.753586827200
H	3.544887329300	0.356802645000	2.753586827200
H	-0.662131859100	-2.032935805800	2.843208664900
H	0.662131859100	2.032935805800	2.843208664900
H	-0.649630170500	-2.039181154300	5.310592058500
H	0.649630170500	2.039181154300	5.310592058500
H	0.000000000000	0.000000000000	6.551317299700
H	-7.853623403900	0.461143808600	1.067801997400
H	7.853623403900	-0.461143808600	1.067801997400
H	-5.501824297000	0.323060568200	1.617705950500
H	5.501824297000	-0.323060568200	1.617705950500

BDP

Symmetry: C_{2v}

C	0.000000000000	-1.217145878900	0.031032412700
C	0.000000000000	1.217145878900	0.031032412700
N	0.000000000000	-1.241522459500	1.427063150000
N	0.000000000000	1.241522459500	1.427063150000
B	0.000000000000	0.000000000000	2.352044455300
C	0.000000000000	0.000000000000	-0.653790406400
C	0.000000000000	-2.567611847600	-0.418867845300
C	0.000000000000	2.567611847600	-0.418867845300
C	0.000000000000	-3.351095556500	0.719376568900
C	0.000000000000	3.351095556500	0.719376568900
F	1.135748817800	0.000000000000	3.158939165500
F	-1.135748817800	0.000000000000	3.158939165500
C	0.000000000000	-2.498899210400	1.835293835600
C	0.000000000000	2.498899210400	1.835293835600
C	0.000000000000	0.000000000000	-2.151648360000
C	0.000000000000	-3.129975883300	-1.812090159800
C	0.000000000000	3.129975883300	-1.812090159800
C	1.201028473100	0.000000000000	-2.852086526200
C	-1.201028473100	0.000000000000	-2.852086526200
C	1.200668054900	0.000000000000	-4.240060492600
C	-1.200668054900	0.000000000000	-4.240060492600
C	0.000000000000	0.000000000000	-4.936684935500

H	0.877894418200	-2.817583692200	-2.375730566500
H	-0.877894418200	-2.817583692200	-2.375730566500
H	0.877894418200	2.817583692200	-2.375730566500
H	-0.877894418200	2.817583692200	-2.375730566500
H	0.000000000000	-4.218294246600	-1.758931291000
H	0.000000000000	4.218294246600	-1.758931291000
H	2.137042182300	0.000000000000	-2.309522676800
H	-2.137042182300	0.000000000000	-2.309522676800
H	2.139882274500	0.000000000000	-4.776993655800
H	-2.139882274500	0.000000000000	-4.776993655800
H	0.000000000000	0.000000000000	-6.018470749000
H	0.000000000000	-4.428320638100	0.757500551100
H	0.000000000000	4.428320638100	0.757500551100
C	0.000000000000	-2.896181001200	3.276656323400
C	0.000000000000	2.896181001200	3.276656323400
H	0.000000000000	-3.981345018900	3.363670208100
H	0.000000000000	3.981345018900	3.363670208100
H	0.878239571000	-2.493381390600	3.779978086900
H	-0.878239571000	-2.493381390600	3.779978086900
H	0.878239571000	2.493381390600	3.779978086900
H	-0.878239571000	2.493381390600	3.779978086900

8.0 Time-resolved EPR spectroscopy of triplet states

Nature of the triplet state and its population

We consider here a triplet state generated by two unpaired electrons, as those produced by ISC mechanism following excitation of an organic molecule.

A triplet state is a state characterized by a total spin quantum number $S=1$; with electron-electron interactions very weak, the state has three degenerate sublevels characterized by a different value of m_s : -1, 0, +1. In triplet states of organic systems, following photoexcitation a pair of electrons is separated in two distinct molecular orbitals (MO). In this system the interaction is normally small-to-large (typically 10^2 - 10^3 MHz). Therefore, the degeneracy is removed by the spin-spin dipolar interaction, characterized by the zero-field splitting interaction:

$$H_{ZFS} = \mathbf{S} \cdot \mathbf{D} \cdot \mathbf{S} \quad (\text{Eq S12})$$

where \mathbf{D} is a traceless dipolar tensor with eigenvalues -X, -Y and -Z; these eigenvalues are related to the energies (X, Y and Z at zero magnetic field) of the sublevels of the triplet T_x , T_y , T_z , eigenstates of the dipolar Hamiltonian. By convention, Z is taken as the (absolute) largest value. Because of the traceless condition for \mathbf{D} , two parameters are enough to represent X, Y and Z:

$$D = -\frac{3}{2}Z; \quad |E| = \frac{|Y-X|}{2} \quad (\text{Eq S13})$$

Photo-generated triplets are high-energy states (with respect to ground state), and consequently they are transient species. The time evolution of the single sublevel population is determined by the balance between the population of the state, that is determined by ISC (see the main text and the Supporting Information Page S34-37), and its depopulation to the ground state, that is another ISC process. Consequently, population of the triplet sublevels is not Boltzmann, and the state is said to be *polarized*. Thermalization of the sublevels is induced by spin relaxation processes (spin-lattice processes), but at low temperature spin-lattice processes and the depopulation of states are 1~3 order of magnitude slower than ISC, which helps for the study of ISC. Magnetic techniques have the proper spectral resolution to study the selective population of the triplet sublevels and can provide information on the ISC process. Here we used Time-Resolved EPR (TREPR).

Time-Resolved EPR

At sufficiently low temperatures, population of the triplet state by ISC is much faster than both spin-lattice relaxation and decay to the ground state; consequently, spectra taken near pulse laser photoexcitation (0.1~1 μs time delay) are rarely perturbed by relaxation processes, and they reflect entirely the ISC processes.

In TREPR, an external magnetic field \mathbf{B} is applied, which removes the degeneracy of the states.

TREPR measures the transitions induced by a microwave field between the levels and obtain information on both the dipolar interaction (related to the relative spin distribution of the two electrons) and the spin polarization (related to ISC).

In a magnetic field, the energy of the triplet sublevels is perturbed because of the Zeeman interaction, characterized by the spin Hamiltonian

$$H_{Ze} = \mu_B \mathbf{S} \cdot \mathbf{g} \cdot \mathbf{B} \quad (\text{Eq S14})$$

where μ_B is the Bohr magneton, \mathbf{S} is the Spin operator and \mathbf{g} the g-tensor.^[9,10]

In this condition, the eigenstates are linear combinations of the three zero-field states, and the combination depends on the orientation of the magnetic field with respect to the dipolar tensor, whose principal reference frame is solid with the molecular frame.

We consider here three specific cases: the magnetic field oriented along the principal directions of \mathbf{D} , $\hat{x} \parallel \mathbf{B}$, $\hat{y} \parallel \mathbf{B}$ and $\hat{z} \parallel \mathbf{B}$.

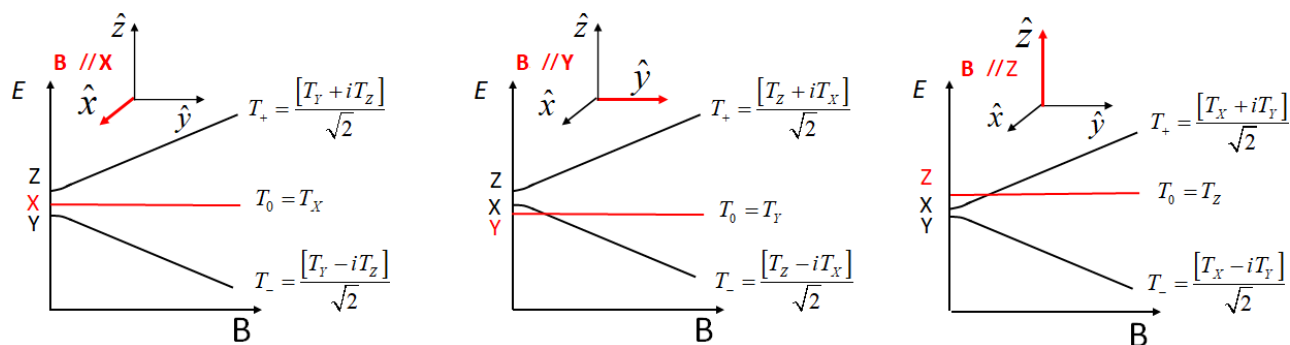


Figure S22. Sketch of the energy variation of the eigenstates of a triplet state ($Z > 0$, as for **IBDP** and **helical-BDP**) in the presence of ZFS interaction as function of the magnetic field for the two cases of $\hat{x} \parallel \mathbf{B}$, $\hat{y} \parallel \mathbf{B}$ and $\hat{z} \parallel \mathbf{B}$. For these particular \mathbf{B} -field orientations, the eigenstates T_+ , T_0 and T_- in the high field approximation are linear combinations of the ZFS states in simple forms.^[11]

By solving the total spin Hamiltonian $H = H_{Zee} + H_{ZFS}$ in the three cases, the energies of the states are obtained (see Figure S22). We observe that one energy level is unaffected by the magnetic field (that along which the magnetic field is oriented), while other two levels are separated in a proportionally way by the magnetic field (at high field).

Rather simple expressions are obtained for the eigenstates in the high-field approximation (ZFS states representation); the expressions are reported in the figure.

In TREPR spectroscopy, allowed transitions are possible between states T_+/T_0 and T_0/T_- . The spectra are recorded at fixed frequency, while looking for the resonance conditions by changing the applied magnetic field (\mathbf{B} modulates the energy difference between the states); therefore, spectra provides EPR intensities as function of the magnetic field. In the case of Figure S22, each of the three field orientation provides a pair of transitions (lines in the spectrum), which are separated, respectively, by the quantities $3X/(\mu_B g_{eff})$, $3Y/(\mu_B g_{eff})$, $3Z/(\mu_B g_{eff})$, where g_{eff} is the effective g-value calculated along that particular direction. These features are visible also in the spectra of powder samples, like in Figure 4b of the main text and, for small anisotropies of g , they are almost symmetric with respect to the center of the spectrum. Therefore, the dipolar interaction is easily obtained from the spectrum.

Information on ISC is, instead, obtained from the polarization of the states, in fact the polarization of the T_+ , T_0 and T_- eigenstates derives from the polarization of the ZFS states.

We can express the eigenstates as function of the ZFS states:

$$T_i = c_X^i T_X + c_Y^i T_Y + c_Z^i T_Z \quad (\text{Eq S15})$$

As a consequence, we can derive that the i -th state receives population from the zero-field states according to the linear combination:^[11]

$$p_{Ti} = |c_X^i|^2 T_X + |c_Y^i|^2 T_Y + |c_Z^i|^2 T_Z \quad (\text{Eq S16})$$

In Figure S23 we give a graphical representation for the case of a population of the *solo* T_X state ($Z > 0$ is considered, in agreement with the Table in Figure 4b, which report $D < 0$) and $\hat{y} \parallel \mathbf{B}$.

The central state is a pure T_Y state (no population), while the other two are equal-weight combinations of T_X (populated) and T_Z (no population), see Figure S22 and Figure S23. In high field, then, the initial population of T_X is equally distributed between T_+ and T_- . The

corresponding two allowed transitions are reported, and they are in emission (*e*, green arrow) or in enhanced absorption (*a*, yellow line). The picture is completed by considering the orientation of the magnetic field along the other two principal directions. We then obtain the bands reported on the right of Figure S23, with the pattern (*e, e, e, a, a, a*).

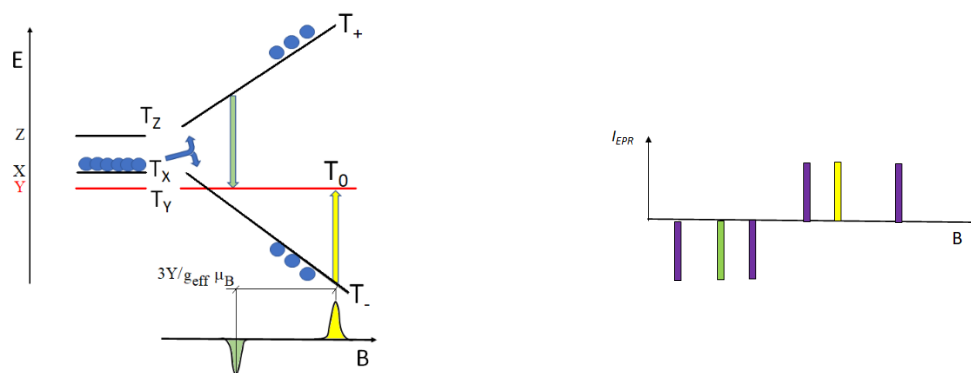


Figure S23. distribution of population for the magnetic field along the Y principal direction, with the selective population of T_x by ISC. In high field the T_x population distributes (blue arrow), according to eq. 1 and the combinations reported in Figure S22, equally distributed between states T_- and T_+ . The resonance conditions (yellow and green arrows) lead to one transition in emission and one in enhanced absorption. The distance between the lines is related to the relative principal value of the \mathbf{D} -tensor. On the right the polarization and the position of bands for the three cases reported in Figure S22, with a (*e, e, e, a, a, a*) pattern.

Because of this tight relation between polarization of high-field states and polarization of ZFS state, a careful simulation of the TREPR spectra allow to obtain both the polarization of the ZFS states by ISC, and the strength of the dipole-dipole interaction, related to the extension of the triplet wavefunction.^[12]

9.0 Synthesis and Molecular Structure Characterization Data

The synthesis of **helical-BDP** was according to literature.^[13] ^1H NMR (400 MHz, CDCl_3): δ = 8.22 (d, 2H, J = 8.0 Hz), 7.95 (d, 2H, J = 8.0 Hz), 7.81 (d, 2H, J = 8.0 Hz), 7.77 (d, 2H, J = 8.0 Hz), 7.66–7.64 (m, 3H), 7.53–7.50 (m, 4H), 7.45–7.42 (m, 2H), 2.06 (s, 6H). MALDI-HRMS($\text{C}_{33}\text{H}_{23}\text{BF}_2\text{N}_2$): calcd. m/z = 496.1922; found m/z = 496.1911.

The synthesis of **sty-IBDP** was according to literature.^[14] ^1H NMR (400 MHz, CDCl_3): δ = 8.18 (d, 2H, J = 16.0 Hz), 7.73 (s, 1H), 7.69–7.66 (m, 5H), 7.55–7.54 (m, 3H), 7.43 (t, 4H, J = 8.0 Hz), 7.37 (d, 2H, J = 8.0 Hz), 7.31–7.29 (m, 2H), 1.46 (s, 6H).

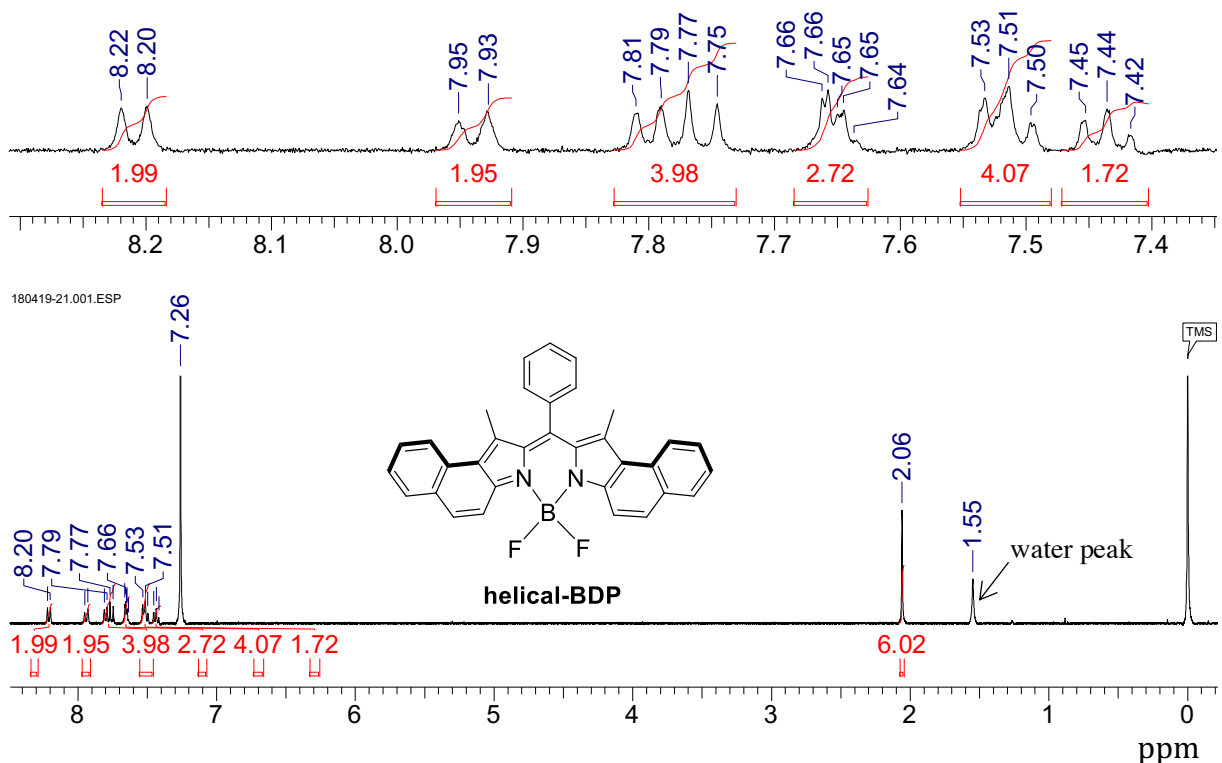
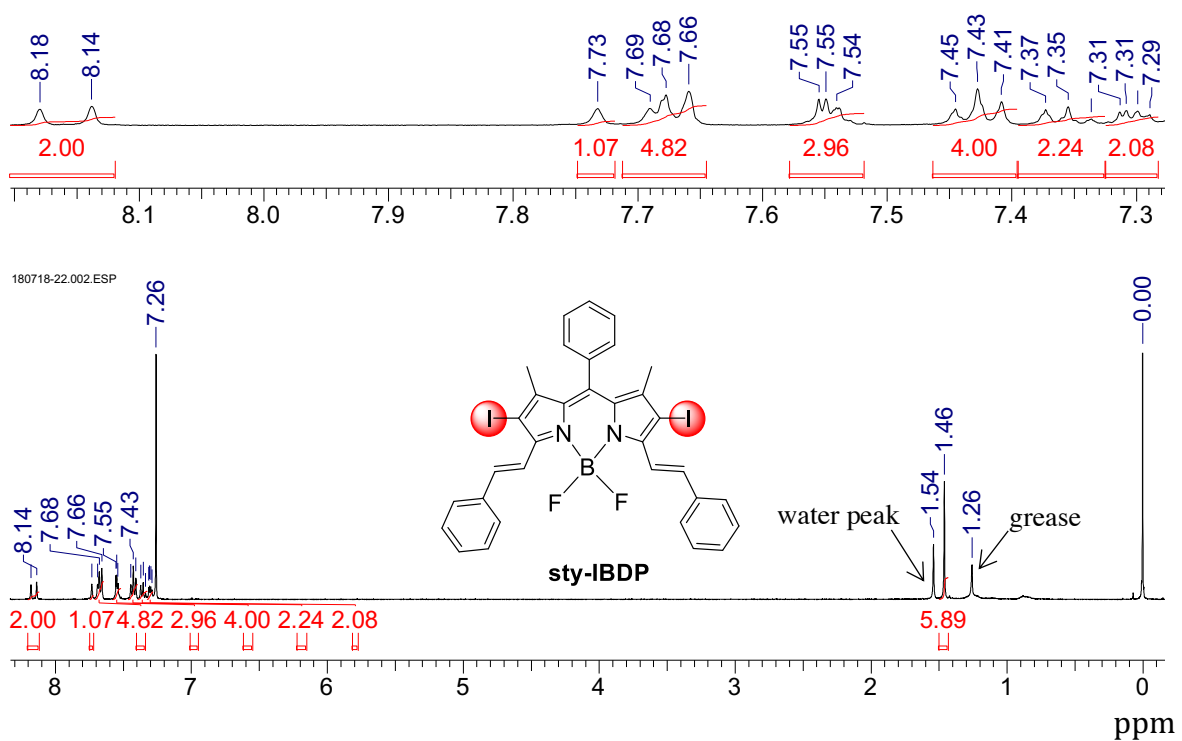
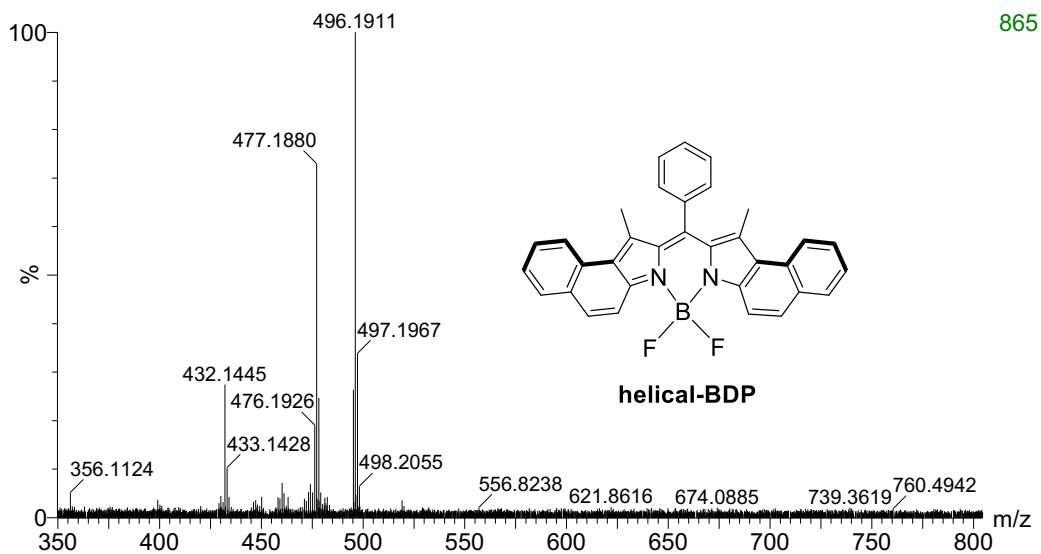


Figure S24. ^1H NMR spectrum of compound **helical-BDP** in CDCl_3 (400 MHz), 25°C.



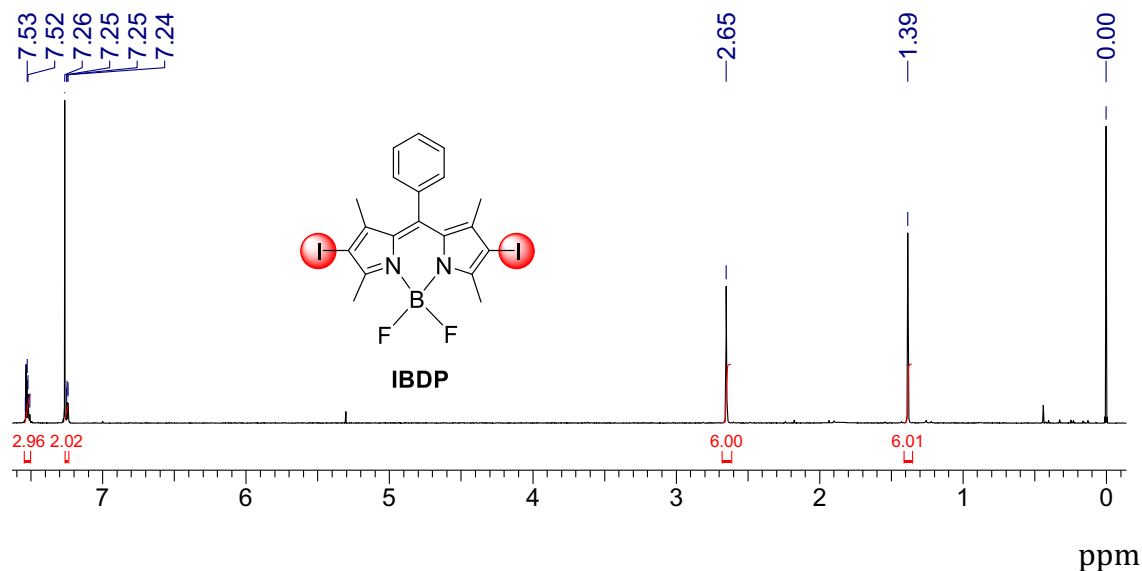


Figure S27. ¹H NMR of compound **IBDP** in CDCl₃ (400 MHz), 25°C.

10.0 References

- [1] Thomas, J. D., Charles, J. G., Barbara, W. H., Giulio, J., David, K., Mladen, K., Johan, M. & Qian, P. Photodynamic Therapy. *J. Natl. Cancer I.*, **90**, 889–905 (1998); Aisling, E. O., William M. G. & Annette T. B. Porphyrin and Nonporphyrin Photosensitizers in Oncology: Preclinical and Clinical Advances in Photodynamic Therapy. *Photochem. Photobiol.*, **85**, 1053–1074 (2009).
- [2] Espenson, J. H. Chemical kinetics and reaction mechanisms (2nd ed.). McGraw Hill. ISBN 9780071139496 (1987).
- [3] Chakraborty, D. K. & Burkhart, R. D. *Macromolecules* **23**, 121–126 (1990).
- [4] Kumar, C., Qin, L. & Das, P. K. Aromatic thioketone triplets and their quenching behaviour towards oxygen and di-*t*-butylnitroxyl radical. *J. Chem. Soc., Faraday Trans. 2*, **80**, 783–793 (1984).
- [5] Wu, W., Sun, J., Cui, X. & Zhao, J. Observation of the room temperature phosphorescence of Bodipy in visible light-harvesting Ru(II) polyimine complexes and application as triplet photosensitizers for triplet-triplet-annihilation upconversion and photocatalytic oxidation. *J. Mater. Chem. C*, **1**, 4577–4589 (2013).
- [6] Olmsted, J. Calorimetric determinations of absolute fluorescence quantum yields. *J. Phys. Chem.* **83**, 2581–2584 (1979).

[7] A. A. Granovsky, Firefly version 8.0.0, <http://classic.chem.msu.su/gran/firefly/index.html> 2014.

[8] M. W. Schmidt, K. K. Baldrige, J. A. Boatz, S. T. Elbert, M. S. Gordon, J. H. Jensen, S. Koseki, N. Matsunaga, K. A. Nguyen, S. Su, T. L. Windus, M. Dupuis, J. A. Montgomery Jr, *J. Comput. Chem.* **1993**, *14*, 1347–1363.

[9] Electron Paramagnetic Resonance: A Practitioners Toolkit, M. Brustolon, E. Giamello (Editors), **2009**, Wiley, Hoboken, New Jersey.

[10] John A. Weil, J. R. Bolton Electron Paramagnetic Resonance: Elementary Theory and Practical Applications, Second Edition, **2007**, Wiley.

[11] Y. Hou, X. Zhang, K. Chen, D. Liu, Z. Wang, Q. Liu, J. Zhao, A. Barbon, *J. Mater. Chem. C*, **2019**, *7*, 12048–12074.

[12] A. Barbon, E. D. Bott, M. Brustolon, M. Fabris, B. Kahr, W. Kaminsky, P. J. Reid, S. M. Wong, K. L. Wustholz, R. Zanre, *J. Am. Chem. Soc.*, **2009**, *131*, 11548–11557.

[13] Z. Zhou, J. Zhou, L. Gai, A. Yuan, Z. Shen, *Chem. Commun.* **2017**, *53*, 6621–6624.

[14] L. Huang, J. Zhao, S. Guo, C. Zhang, J. Ma, *J. Org. Chem.* **2013**, *78*, 5627–5637